coatings

MDPI

*Article*

# An Alternative Methodology for the Evaluation of Photocatalytic Activity of Polymeric Coatings by Monitoring Dye Degradation

**Xabier Sandua [1,2,*], Pedro J. Rivero [1,2], José F. Palacio [3], Joseba Esparza [3] and Rafael Rodríguez [1,2]**

[1] Engineering Department, Campus Arrosadía s/n, Public University of Navarre, 31006 Pamplona, Spain
[2] Institute for Advanced Materials and Mathematics (INAMAT2), Campus Arrosadía s/n, Public University of Navarre, 31006 Pamplona, Spain
[3] Centre of Advanced Surface Engineering, AIN, 31191 Cordovilla, Spain
* Correspondence: xabier.sandua@unavarra.es

**Abstract:** This work provides an alternative method for evaluating the photodegradation behaviour of different types of dyes such as Methylene Blue, Rhodamine B, Congo Red, Metanil Yellow, and Malachite Green. In this methodology, the coating is dyed with the chosen colorant and two beams of light are combined and channelled to a spot on the dyed coating through an optical fibre, the first one from an ultraviolet (UV) source (which is the responsible of activating photocatalysis) and the second one from a Visible light source, which is employed to monitor changes in colour along the time. The photocatalytic coating selected for testing this methodology consists of a mat of electrospun poly (acrylic acid) (PAA) fibres that acts as base film, furtherly coated by using layer-by-layer (LbL) assembly technique for the immobilization of two different photocatalytic metal oxide precursors ($TiO_2$ and $Fe_2O_3$) nanoparticles. The morphological characterization of the samples has been implemented by means of scanning electron microscopy (SEM), confocal microscopy, and water contact angle measurements in order to analyse the resultant thickness, roughness, electrospun fibre diameter, and wettability. The experimental results clearly demonstrate the validity of the methodology to measure the photocatalytic activity in all dyed coatings, although significant differences have been observed depending on the selected dye.

**Keywords:** photocatalysis; dyes; electrospinning; layer-by-layer assembly; metal oxides; coatings



**Citation:** Sandua, X.; Rivero, P.J.; Palacio, J.F.; Esparza, J.; Rodríguez, R. An Alternative Methodology for the Evaluation of Photocatalytic Activity of Polymeric Coatings by Monitoring Dye Degradation. *Coatings* **2022**, *12*, 1529. https://doi.org/10.3390/coatings12101529

Academic Editor: Mariaenrica Frigione

Received: 15 September 2022
Accepted: 7 October 2022
Published: 12 October 2022



## 1. Introduction

The photocatalytic activity of particles and fibres can be easily monitored by dissolving them in an aqueous solution of methylene blue. In the case of coatings [1], however, the contact area between coating and dye solution is relatively smaller than in a suspension of particles or fibres and, thus, the degradation time of the overall dye in the solution is very long and can lead to a number of practical problems such as solvent evaporation, changes in concentration, or inhomogeneities in the system. An alternative method that would allow one to get rid of these problems would be to carry out this kind of test in a dry environment by acting of previously dyed coatings. This alternative method uses a visible light source (so that the reduction of methylene blue spectrum could be appreciated during the essay) and a UV light source (so as to activate the photocatalytic reactions in the coating). This idea has been successfully employed by the authors in a previous work [2], and the present article aims to look deeper in this this strategy and extend it to a wide range of dyes in addition to Methylene Blue.

According to its chemical structure, dyes are divided into azo, nitro, nitrous, diarylmethane, triarylmethane, xanthene, anthraquinoid, acridine, cyanine, quinone-imine, pthalocyanine, and thiazole, among others [3]. This study centres the attention in five types of dyes with a different chemical structure. Congo Red (CR) is one of the most

common employed azo-dyes [4] and Malachite Green (MG) is a triarylmethane type of dye [5]. An example of xanthene dye is Rhodamine B (RhB) [4] and Methylene Blue (MB) is a heteropolyaromatic dye [6]. The last studied azo-dye is Metanil Yellow (MY) [7]. Figure 1 presents the resultant chemical structures of all of the dyes used in this study.

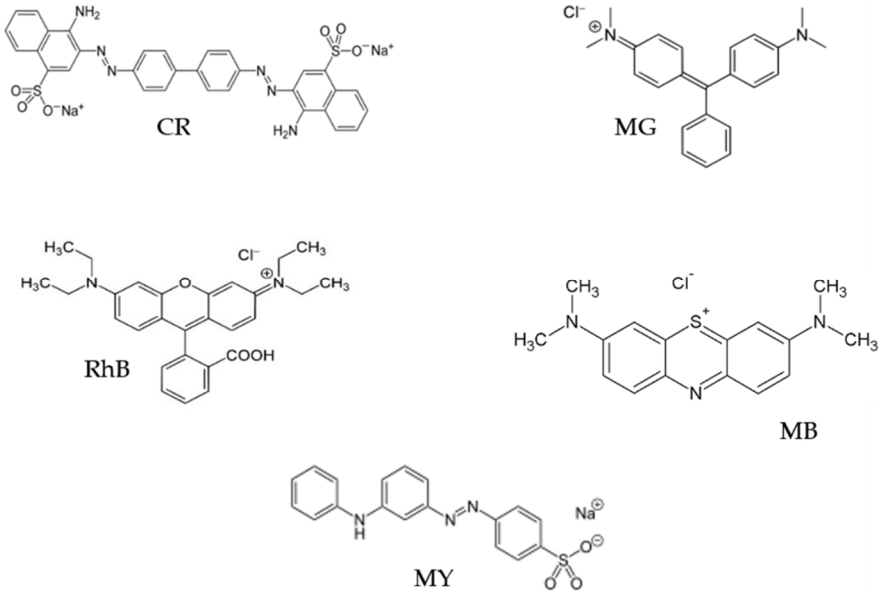


**Figure 1.** Chemical structure of all of the dyes used in this study such as Congo Red (CR), Malachite Green (MG), Rhodamine B (RhB), Methyl Blue (MB), and Metanil Yellow (MY), respectively.

Photocatalysis is considered an eco-friendly method, and no sludge is produced in the colorant removal process [8]. One of the most widely known compounds employed in this specific photochemical method is titanium dioxide ($TiO_2$). When this metal oxide precursor is illuminated under UV light (around 380 nm), an electron is excited to the conduction band, leaving a hole in the valence band of the $TiO_2$ [9]. This phenomenon chemically produces hydroxyl radicals which act as oxidating agents to transform organic matter (i.e., dyes) to non-toxic species such as $CO_2$ and $H_2O$ [10]. Then, the presence of sulphur heteroatoms in dyes are transformed to ($SO_4^{2-}$) [11], and nitrogen mineralization is conducted. Amino groups are released by means of an oxidative process, creating $NH_4^+$. Afterwards, $NO_3^-$ ions are produced [12].

One of the parameters which directly affects the degradation rate of a dye using $TiO_2$-based photocatalysis is the dopant content effect [13]. In this sense, by combining $TiO_2$ with other semiconductor oxides, the resultant photocatalysis efficiency is enhanced by narrowing the band gap of $TiO_2$ [14]. This fact is due to the $Fe^{3+}$ separation capacity of photo-generated electron-hole pairs. According to this, several recent works can be found based on the combination of $TiO_2$ and $Fe_2O_3$ in dye degradation applications [15]. More specifically, $Fe_2O_3$ is a perfect candidate in surface catalysts due to its abundance, stability and matched band position with $TiO_2$ for efficient charge separation [16], this last one being the main reason for having been chosen as an ideal dopant of $TiO_2$ in this work. Moreover, these two types of metal oxide precursors interact with light in a different way for photocatalytic applications since $TiO_2$ has its maximum peak of absorbance in a wavelength (388 nm), whereas $Fe_2O_3$ has its maximum peak in the visible spectrum (620 nm), respectively [17,18]. Furthermore, there is much recent research addressing that the incorporation of $Fe_2O_3$ particles to the coating has influence in $TiO_2$ particle size and photocurrent responses under a UV light source irradiation [19]. The latest articles about enhancing photocatalytic activity employ this couple of metal oxide so as to eliminate organic pollutants since it presents an effective low cost method [20].

In this work, the functional coatings have been performed by combining two fabrication techniques such as the electrospinning and layer-by-layer assembly, which make

possible a great immobilization of all dyes of this study. In addition, the combination of both deposition techniques provides new features to the functional surface, compared to the coatings that could be achieved separately with these techniques. The polymeric matrix obtained by the electrospinning process makes it possible to achieve an homogeneous structure with a good adhesion onto the reference substrate, whereas the LbL assembly provides a good affinity towards the electrospun fibres with a good control over the thickness coatings and dispersion of the metal oxide particles [21,22]. To the best of our knowledge, this is the first time the photocatalytic response of these dyes, with different chemical structures between them, are evaluated under this experimental test.

## 2. Materials and Methods

### 2.1. Materials

Poly (acrylic acid) (PAA; Mw ≈ 450,000), β-cyclodextrin (β-CD, purity 98%) and ethanol (99%) have been used for the electrospinning process. In the layer-by-layer assembly, titanium oxide ($TiO_2$, pure anatase nanopowder < 25 nm) has been diluted into an aqueous solution of poly (diallyldimethylammonium chloride) (PDDA; Mw ≈ 100,000 and 20wt% in $H_2O$), whereas iron oxide ($Fe_2O_3$, <5 μm) particles have been diluted into an aqueous solution of poly (sodium 4-styrenesulfonate) (PSS; Mw ≈ 70,000), respectively. As dyes, Methyl Blue (1.5wt% in $H_2O$), Metanil Yellow (70% dye content), Rhodamine B (>95% dye content), Congo Red (>35% dye content) and Malachite Green (Oxalate Salt) have been used. All of the chemicals have been provided from Sigma-Aldrich (St. Louis, MO, USA). Finally, standard glass slides with a dimension of 75 × 50 $mm^2$ have been used for the fabrication of the functional coatings.

### 2.2. Functional Coatings Deposition

For the preparation of the photocatalytic functional coatings, three well-differentiated steps have been performed, as it is explained in the following paragraphs.

#### 2.2.1. Electrospinning Process

In a first step, a base of electrospun fibres mat have been performed by using the electrospinning process [23]. This technique is based on the transformation from a viscoelastic fluid into electrospun fibres, applying a high-voltage supply in the tip of a syringe where the polymeric solution is pumped out [24,25]. Among all of the operative parameters, three of them have to be perfectly controlled in order to obtain the desired "Taylor Cone" in the tip of the syringe: the flow rate of the solution, the applied voltage between the syringe tip and collector, and the tip-collector distance [26,27]. In this work, a viscous solution of PAA has been selected as polymeric precursor using ethanol as solvent, whereas β-CD has been used a crosslink agent in a further thermal treatment. A total weight of 0.8 g of PAA and 0.128 g of β-CD have been added to a 11.6 mL of ethanol and it is stirred for 24 h at room temperature to obtain a high density solution [2]. In order to perform the electrospinning coating, the polymeric solution has been placed in a 20-gauge needle with an inner diameter of 0.6 mm. A high-voltage of 15 kV has been applied between the tip of the syringe and the base where the sample is placed, with a tip-collector distance of 15 cm and a flow rate of 1.3 mL/h, respectively. Once the electrospun fibres mat has been deposited onto the reference substrate, a heat treatment process of 180 °C during 40 min has been carried out in order to promote the chemical crosslinking of the electrospun fibres, and as a result a great degree of insolubility and better chemical stability is obtained [2].

#### 2.2.2. Layer-by-Layer Assembly Process

In a second step, layer-by-layer assembly technique has been performed onto the electrospun fibre mat samples. This deposition technique offers superior control and versatility when compared to other thin-film deposition techniques [28], making possible a suitable dispersion of the metal oxide precursors through the polyelectrolytes during the fabrication of the multilayer structure [29,30]. In this technique, thin-films are formed

by alternatively immersion of the substrate in oppositely charged polyelectrolytes [31]. Depending on the charge density, these polyelectrolytes can be classified as weak or strong polyelectrolytes [32,33]. In this work, strong polyelectrolytes such as PDDA (polycation) and PSS (polyanion) have been selected for being effective encapsulating agents for the metal oxide precursors [34]. A 10 mM solution of PDDA in 250 mL of ultrapure water has been prepared, and after a stirring time of 2 h, 250 mg of $TiO_2$ has been added, which has been stirred for 3 h and then, an ultrasonication process of 1 h has been carried out. Then, 10 mM solution of PSS in 250 mL of ultrapure water has been also prepared, and after stirring time of 2 h, $Fe_2O_3$ powder has been added, which has been stirred for 3 h and ultra-sonicated for 1 h, respectively.

Finally, by using the LbL assembly, a correct dispersion of the metal oxide precursors has been achieved in the polyelectrolyte solutions [35–37]. Intermediate distilled water solutions have been also employed in order to perform washing steps of the samples. All of the solutions have been adjusted to a pH of 2.0 in order to obtain a desired thin-film thickness [38]. The combination of a positive layer and a negative layer is denoted as bilayer. Previous studies have indicated that a thickness corresponding to a final number of five bilayers in each sample preparation is considered as appropriate for the photocatalytic efficiency.

#### 2.2.3. Immobilization Dyes Deposition Process

As it has been previously mentioned, five types of dyes have been deposited onto the previous fabricated coatings in order to carry out the photocatalytic tests and, thus, their different photocatalytic responses have been evaluated. In this sense, the outer layer of the functional coatings is the negative charged polyelectrolyte (PSS) where its superhydrophilic feature facilitates the resultant adhesion of the dyes into the coating [39]. With the aim of obtaining a similar absorbance value of all spectra dyes, as it is shown in the photocatalytic experiments, the immersion time is varied for each dye of this study. More specifically, in the case of CR, the samples are introduced into 12 mM aqueous solution of this dye, and after that, the sample is heated to 50 °C and stirred for 2 h, respectively. For the immobilization of MG, 6.25 mM aqueous solution of this dye has been stirred for 1 h at room temperature and then, the sample is immersed in this solution until the desired absorbance of its spectrum is obtained. In the cases of RhB, MB, and MY dyes, 6.25 mM aqueous solutions of these dyes have been prepared and stirred for 2 h. Then, the samples have been immersed in these dyes for a period time of for 10 s, 2 h, and 60 s, respectively. All of the dyes solutions were at their natural pH value. In order to have a better understanding of the whole process, in Figure 2 is shown a schematic representation of the three specific steps for the preparation of the functional coatings with the immobilized dyes.

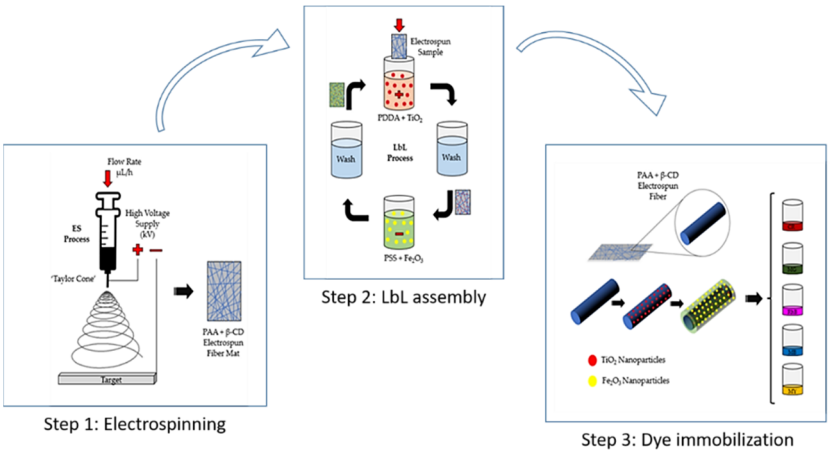


**Figure 2.** Schematic representation of the three different steps for the fabrication process of the functional coatings by the combination of the electrospinning and LbL assembly techniques.

### 2.3. Characterization Techniques

Water contact angles have been measured using Theta (Attension) optical tensiometer (CAM 100 KSV Instruments, Burlington, VT, USA). Sessile drops are recorded in fast mode with a trigger, after 5 s from the moment the drop touched the surface. Contact angles have been measured using the tangent algorithm drop profile fitting method. An average of 30 frames/s has been used to calculate the contact angle for each drop. Each water contact angle value is obtained as an average of three measurements performed at different locations on the coatings.

A field emission-scanning electron microscopy (FE-SEM Hitachi S4800, Tokyo, Japan) has been used to appreciate the surface morphology of the samples. The thickness and roughness values have been numerically measured by a confocal microscopy (model S-mart, SENSOFAR METROLOGY, Barcelona, Spain) with an objective of EPI 50× v35 for a final area of 340.03 × 283.73 $\mu m^2$, respectively.

The absorbance spectra of the dyes have been analyzed by a Jasco V-730 (Agilent, Santa Clara, CA, USA), whereas the chemical information about the presence of functional groups of the samples has been determined by a Fourier-transform infrared (FTIR, Perkin Elmer, MA, USA) spectroscopy study, using a Perkin Elmer Frontier spectrophotometer (Waltham, MA, USA) in the spectra range of 600–4000 $cm^{-1}$.

Finally, the photocatalytic tests have been performed by using UV-VIS optical fibres of 200 µm and Ocean Optics USB2000 (Ocean Insight, FL, USA), whereas the visible light (Takhi-HP, Pyroistech) and UV light (COB365, Pyroistech, Navarra, Spain) have been used as the main sources light, respectively.

### 2.4. Photocatalytic Test

For the photocatalytic efficiency determination, the optical transmission setup used in previous works has been employed [2,40]. More specifically, both UV (maximum spectra at λ = 365 nm) and visible light sources have been connected to a bifurcated optical fibre, which is in charge of guiding both light irradiation to the holder where the functional coatings with the immobilized dyes (samples) are perfectly placed. The transmitted light has been guided by an optical fibre to the spectrometer, and this device is connected to the spectroscopy computer software, in order to evaluate the photodegradation over the time. The visible light makes possible to visualize dye spectrum and also activates $Fe_2O_3$ particles, whereas UV light is in charge of activating $TiO_2$ particles, which is the main photocatalytic compound [41]. The test has been performed for a maximum period of 20 h with an incident area in the dye sample of 12.56 $mm^2$, respectively. This essay is represented in Figure 3.

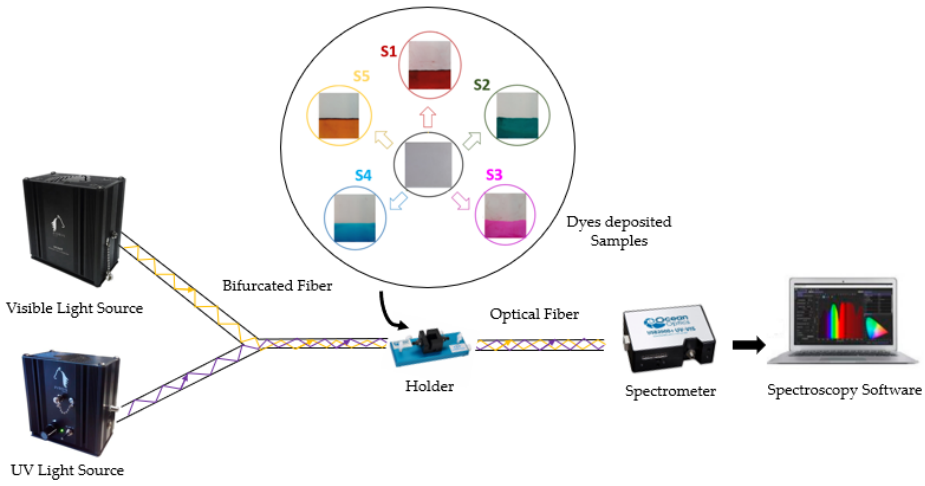


**Figure 3.** Schematic representation of the photocatalytic test.

## 3. Results and Discussion

### *3.1. Characterization of the Functional Coatings*

First of all, in Table 1 presents the resultant nomenclature corresponding to the fabrication of the coatings in the initial steps (step 1 and step 2, respectively). More specifically, the sample denoted as REF corresponds to the PAA + β-CD electrospun fibres (only electrospinning process), whereas the ones denoted as S0 and S01 correspond to the samples, which combine both electrospinning and LbL assembly techniques. The main difference between them is that S0 only contains polyelectrolytes (PDDA and PSS) onto the elecrospun fibres, whereas S01 uses these same polyelectrolytes as effective encapsulating agents of the metal oxide precursors ($TiO_2$ and $Fe_2O_3$) during the LbL assembly process.

**Table 1.** Summary table of the analysed functional coatings before dyes immobilization.

| REF | S0 | S01 |
|---|---|---|
| PAA + β-CD | PAA + β-CD//PDDA/PSS | PAA + β-CD//PDDA + $TiO_2$/PSS + $Fe_2O_3$ |

Figure 4 shows the resultant SEM images of the three analysed functional coatings. In Figure 4a can be appreciated the electrospun fibres mat obtained by the electrospinning technique (step 1 of the fabrication process). All of these fibres are homogenous, showing a uniform dispersion among the matrix, although some beads are also formed due to certain instabilities during the deposition process [42]. These instabilities may appear due to the effects of the employed variables in the electrospinning process. In this case, an inadequate evaporation of the solvent during the electrospinning process may be the main cause of production of beads [43]. In Figure 4b it can be perfectly observed a great difference in the aspect of the coatings after performing the layer-by-layer assembly, showing an increase in the fibre diameter due to the alternate deposition of the oppositely charged polyelectrolytes. In Figure 4c,d, it can be appreciated the SEM images of the samples after immobilization of the metal oxide precursors (bright colour spots) during the LbL assembly (step 2 of the fabrication process) at different magnification (100 and 50 μm, respectively). One main conclusion which can be derived is that these metal oxide precursors are randomly distributed with a certain degree of aggregation along the multilayer structure during this step associated to the LbL assembly. Finally, in order to corroborate the presence of these metal oxide precursors in the outer surface of the coatings, EDX (Hitachi S4800, Tokyo, Japan) is presented in Figure 4e where the location of the peaks related to Ti (mostly in 4.5 keV) and Fe (mostly 6.4 keV), elements associated to the oxides, can be observed along the spectra. In Figure 4f is shown the $TiO_2$ and $Fe_2O_3$ particle distribution along the coating, where $Fe_2O_3$ particles are marked in green colour and $TiO_2$ particles are marked in red colour, respectively.

The intrinsic properties associated to the wettability, fibre diameter, and roughness of the functional coatings have been also analysed, as it can be appreciated in Figure 5. It is well-known that the resultant wettability of a surface depends on the roughness and heterogeneity of the deposition as well as on the relationship between shape and size of the immobilized particles [44]. In addition, the features related to the outermost surface layer directly affect to the resultant wettability property of the functional coating [45,46]. In this work, the outermost layer of the samples (REF, S0 and S01) contain polyelectrolytes of superhydrophilic behavior such as PAA [46] and PSS [47], respectively. After observing Figure 5a, the samples corresponding to REF and S0 have shown low values of the water contact angle, although S0 sample has a greater value than REF sample since LbL immersion process makes the film to absorb water, and as a result, the wettability is decreased after LbL process. More specifically, the REF sample as it is only composed of electrospinning coating has shown a greater tendency to absorb water, which is associated to the hydroxyl groups of the PAA, and as a result, a superhydrophilic behavior is clearly obtained. In addition, it is widely known the superhydrophilic effect that UV light has in photocatalytic metal

oxide precursors doped coatings [48–50]. However, the presence of metal oxides particles such as $TiO_2$ and $Fe_2O_3$ on the functional coating without having been illuminated with external light sources, has not shown a reduction in the resultant wettability [51]. In this work, the water contact angle measurements have increased from 1.6° ± 0.5° in the case of REF, 25.3 ± 2.3 for S0 up to a value of 66.9 ± 1.2 in the case of S01 (see Figure 5a). In terms of fibre diameter, after performing the layer-by-layer assembly, the alternate deposition of oppositely charged polyelectrolytes has produced an increase in the resultant diameter (see Figure 5b), this effect being more notorious in the sample composed of the photocatalytic metal oxides than in the functional matrix [40]. The corresponding fibre diameter has been from 2.2 ± 0.3 µm (REF), 3.1 ± 0.4 µm (S0) up to 5.1 ± 0.6 µm (S01). Finally, by means of confocal microscopy, a roughness parameter such as arithmetical mean height (Sa) has been also studied (see Figure 5c). As the sample thickness is increased as a function of the addition of the multilayer structure associated to the LbL assembly process, a less rough surface is obtained as it can be appreciated for the S0 (0.8 ± 0.1 µm) and S01 (0.5 ± 0.08 µm) samples in comparison with REF (1.3 ± 0.1 µm), respectively. The experimental results indicate that LbL process significantly increases the electrospun fibre diameters by the deposition of successive charged polyelectrolytes (PDDA and PSS) onto the fibre surface, and the typical porous structure of an electrospinning sample is modified, allowing a more homogeneous and uniform surface coating.

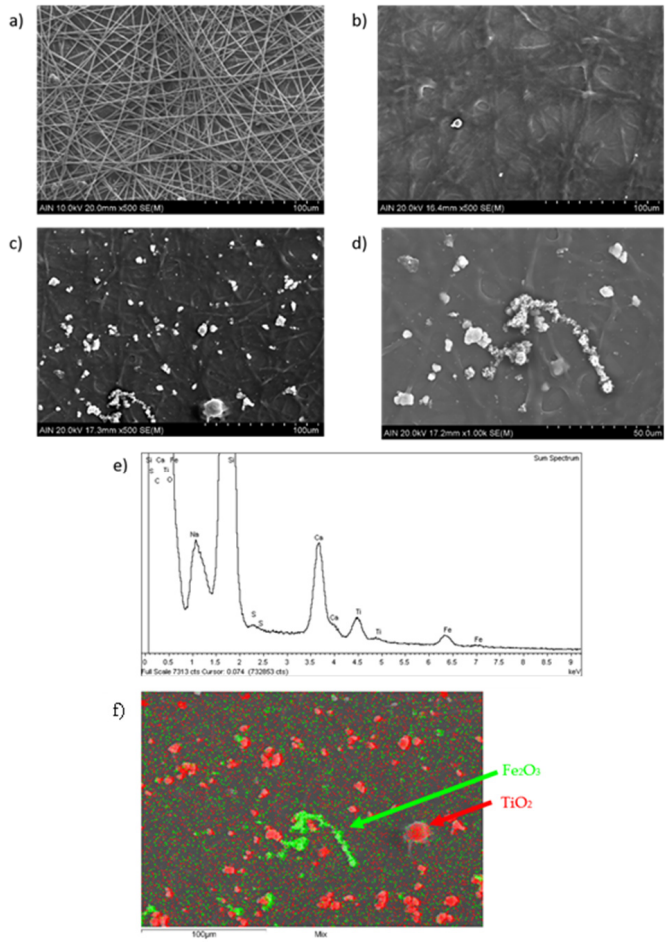


**Figure 4.** SEM images of the functional coatings composed of (**a**) only electrospun PAA + β-CD fibres (REF) (**b**) combination of PAA + β-CD//PDDA/PSS (S0) and (**c**,**d**) combination of PAA + β-CD//PDDA + $TiO_2$/PSS + $Fe_2O_3$ (S01); (**e**) EDX analysis of the sample S01 with the presence of Ti and Fe peaks, respectively; (**f**) EDX 2D mapping of the sample S01 with the presence of $Fe_2O_3$ and $TiO_2$ particles.

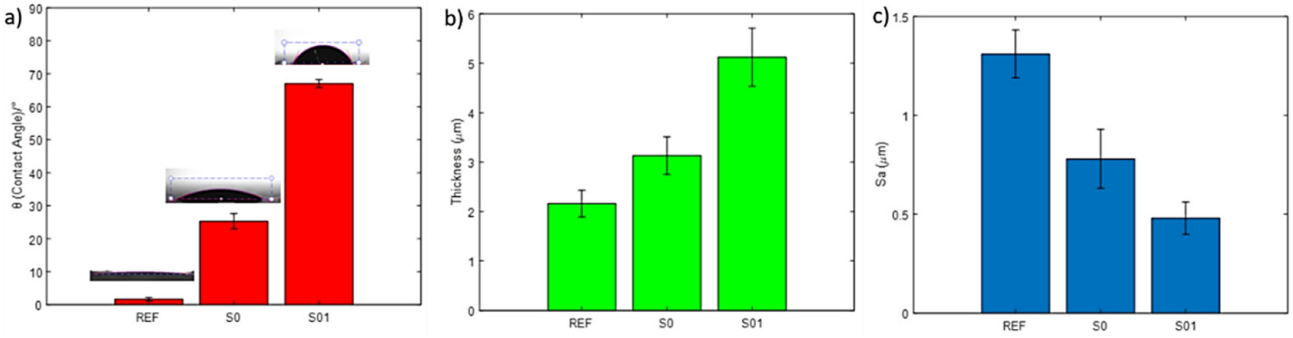


**Figure 5.** Water contact angle value measurements (**a**), thickness value measurements (**b**) and roughness value measurements (**c**) for PAA + β-CD fibre (REF), PAA + β-CD//PDDA/PSS (S0) and PAA + β-CD//PDDA + $TiO_2$/PSS + $Fe_2O_3$ (S01), respectively.

### *3.2. Dyes Immobilization onto the Functional Coatings*

The samples are denoted as S1 for the Congo Red (CR), S2 for the Malachite Green (MG), S3 for the Rhodamine B (RhB), S4 for the Methylene Blue (MB), and S5 for the Malachite Yellow (MY), respectively. Figure 3 shows the final aspect of the photocatalytic functional coatings after the dyes immobilization, being the reference S01 sample (PAA + β-CD//PDDA + $TiO_2$/PSS + $Fe_2O_3$) in the center of the image.

The absorbance measurements of all of the dyes have been also performed in order to compare their photocatalytic response after light irradiation. In Figure 6 is shown the normalized spectra and it and the maximum absorbance values are located at different wavelength position in the visible region spectra from 400 to 700 nm. According to this, the sample S1 of CR has shown a main broad peak located at 500 nm [52]. The sample S2 of MG has shown two distinctive peaks at well-separated wavelengths, being the lower intensity peak located at 425 nm and the higher intensity peak located at 640 nm [53], respectively. The sample S3 of RhB has shown a narrow peak located at 570 nm [54]. The sample S4 of MB have shown two different peaks nearly located at 620 and 670 nm, showing the last one a slight absorbance intensity [55]. Finally, the sample S5 of MY has shown a broad peak with its maximum centred around 440 nm [56]. Some dyes may present a slight variation from their original wavelength value. This can be a result of the pH of the dye solutions where the samples were introduced [57].

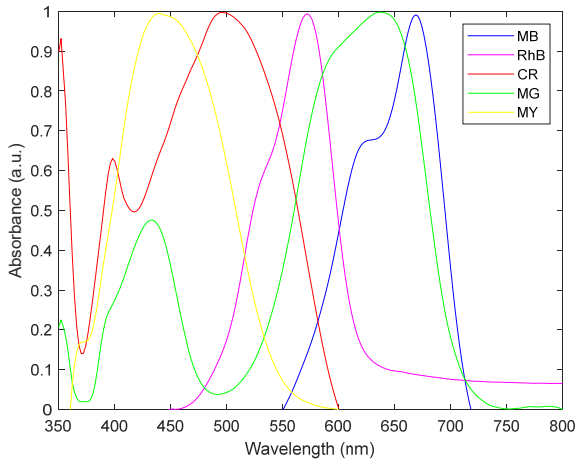


**Figure 6.** UV-VIS spectra of all of the dyes of this study with their maxima absorbance peaks located at different wavelength position from 425 to 670 nm.

### *3.3. Photocatalytic Activity*

The photocatalytic tests have been performed for all of the dyes in concordance with the setup previously commented in the experimental section. First of all, in order to

have a better evaluation of the photocatalytic effects related to the metal oxide precursors immobilized into the samples, two different tests have been carried out for each dye, respectively. The first one is performed for the dye directly deposited onto S0 sample (no presence of metal oxides), in order to observed the degradation of the colorant by means of UV light without any photocatalytic interaction. The second one is conducted for the dyes directly deposited onto the functions coating S01 corresponding to the samples from S1 up to S5 with the aim of studying the resultant degradation of the dyes in the presence of photocatalytic precursors such as $TiO_2$ and $Fe_2O_3$. In addition, in order to see the local discoloration of the samples after light irradiation, an optical image has been taken for a visual analysis. Finally, the evolution of the FTIR spectra has been also performed in order to corroborate the photocatalytic activity of the samples by observing a gradual decrease related to IR transmittance peaks of the functional groups of the immobilized dyes.

In Figure 7, the whole photocatalytic tests performed to CR azo-dye is shown. According to this, Figure 7a indicates the resultant degradation rate of the samples without any presence of metal oxides, and it can be observed that the dye has the tendency of degrading by the self-effect of the UV-light or by a residual photocatalytic activity of the base element, reaching a degradation rate of 35%, respectively. However, an important difference has been observed for the samples with the presence of the metal oxides (S1) since the degradation rate of the CR azo-dye immobilized in the coating is almost 80% (see Figure 7b) at the same experimental conditions. In Figure 7c the resultant discoloration of the dye in a micrometric incident area (12.56 $\mu m^2$, bright aspect) after 20 h of testing is shown. In addition, in Figure 7d is shown the FTIR spectra previous and after irradiation photocatalytic test. The stretching of N-H and C-H groups can be observed in 3344 and 2923 $cm^{-1}$ peaks, respectively. The stretching vibration band of the azo group N=N appears in wavenumbers of 1554 $cm^{-1}$ [58]. The asymmetry stretching vibration of S-O group can be appreciated due to the transmittance peak at 1405 $cm^{-1}$ [59]. Finally, 1172 and 1042 $cm^{-1}$ peaks correspond to C-N stretching functional groups. After carrying out the photocatalytic tests, all of the transmittance peaks have shown a decrease in their corresponding intensities of the mentioned functional groups of CR, which can be associated with the possible production of free radicals during the photocatalytic test [60].

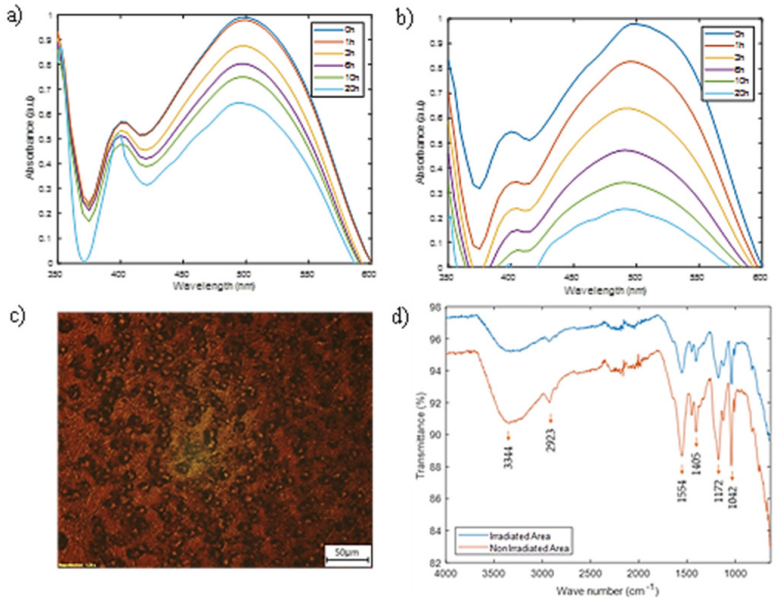


**Figure 7.** (**a**) Evolution of the degradation rate of CR deposited into S0 sample for a total irradiation time of 20 h; (**b**) evolution of the degradation rate of CR deposited into S1 sample for a total irradiation time of 20 h; (**c**) optical microscopy image of a micrometric degraded area of the dye; (**d**) FTIR spectra of the irradiated and non-irradiated area of the Congo Red sample.

In Figure 8, the whole photocatalytic tests performed on the MG dye are shown. According to this, Figure 8a indicates that the irradiation light onto the sample without any metal oxide precursors has shown a less degradation (around 20%) of the green colorant in comparison with CR dye. In addition, in Figure 8b is shown the resultant degradation of the green dye immobilized onto the sample composed of the metal oxide precursors (S2), achieving a total photodegradation of more than 80% with the corresponding disappearance of the two well-distinguished peaks of the MG dye. In Figure 8c, the resultant discoloration of the MG dye with a clear spherical shape after light irradiation of 20 h, respectively, is shown. In Figure 8d the FTIR spectra before and after light irradiation of MG sample is shown, and it can be conclude that there is almost a total reduction of the transmittance peak intensity of the functional group related to aromatic C-H stretching at 2967 $cm^{-1}$, which is a representative peak for this type of triarylmethane dye [61]. In addition, other representative peaks of this dye such as at 1702 $cm^{-1}$ (C=O), 1586 $cm^{-1}$ and 1447 $cm^{-1}$ (aromatic C-C stretching in ring), 1365 $cm^{-1}$ and 1158 $cm^{-1}$ (C-H bending) and 839 $cm^{-1}$ (aromatic C-C stretching) have also been presented [62,63]. An important reduction in their corresponding intensities or even a total disappearance of them has been obtained after testing, which can be associated to the production of free radicals by the photocatalytic phenomena in the functional surface of the sample.

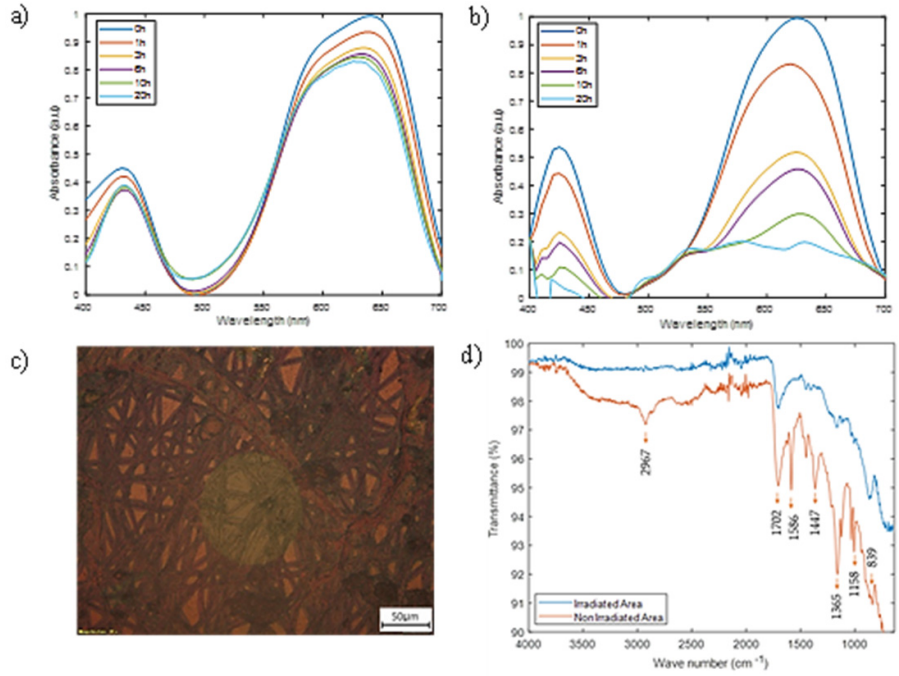


**Figure 8.** (**a**) Evolution of the degradation rate of MG deposited into S0 sample S0 for a total irradiation time of 20 h; (**b**) evolution of the degradation rate of MG deposited into S2 sample for a total irradiation time of 20 h; (**c**) optical microscopy image of a micrometric degraded zone of the dye; (**d**) FTIR spectra of the irradiated and non-irradiated area of the Malachite Green sample.

In Figure 9 the whole photocatalytic tests performed to RhB dye are shown. As has occurred with CR sample, RhB has shown an important degradation of around 40% in the sample without metal oxides (Figure 9a), although this effect is more notorious for the samples composed with the photocatalytic precursors (S3) where it is almost completely degraded (around 95%, Figure 9b). In Figure 9c is shown the resultant discoloration of the doped fibre with a clearly circular micrometric area, whereas in Figure 9d the FTIR spectra of the RhB sample before and after the photocatalytic essay are shown. A C-H stretching vibration, typical of this type of colorant, can be observed at 2925 and 2850 $cm^{-1}$. A strong peak of C=O stretching vibration is presented at 1697 $cm^{-1}$ [64], whereas the dual peak at 1448 and 1406 $cm^{-1}$ corresponds to an aromatic stretching of C-C [65]. In addition, a

smooth peak at 1220 $cm^{-1}$ indicates a C-N bond, whereas the vibration at 1162 $cm^{-1}$ is related to S-O group of sulfonate [66]. In all of the cases, the intensities related to these peaks have been reduced after light irradiation.

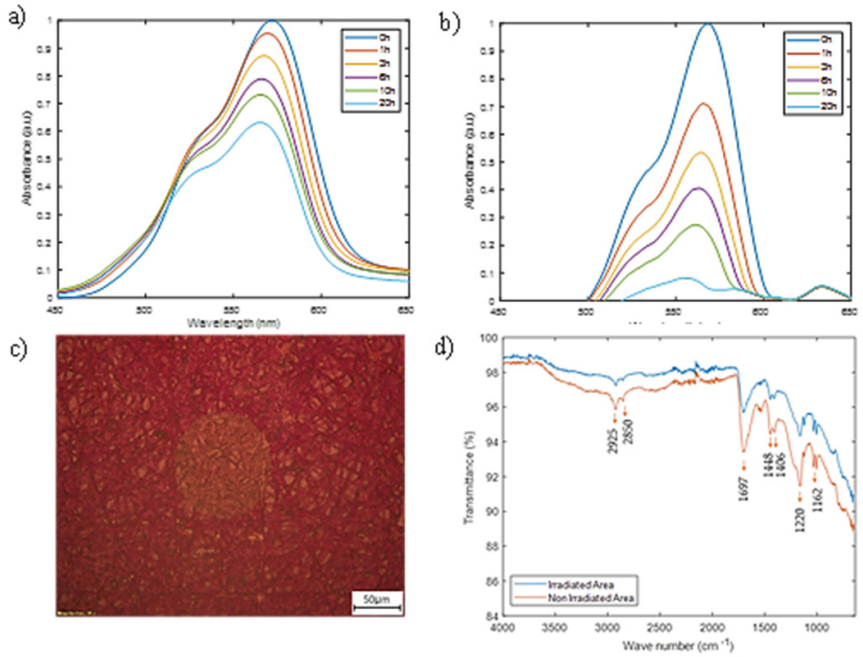


**Figure 9.** (**a**) Evolution of the degradation rate of RhB deposited into S0 sample S0 for a total irradiation time of 20 h; (**b**) evolution of the degradation rate of RhB deposited into S3 sample for a total irradiation time of 20 h; (**c**) optical microscopy image of a micrometric degraded zone of the dye; (**d**) FTIR spectra of the irradiated and non-irradiated area of Rhodamine B sample.

In Figure 10 the whole photocatalytic tests performed to MB dye are shown. The behavior of this specific dye has been previously studied by identical photocatalytic test conditions in our previous studies [2,46]. The experimental results indicate that the coloration degradation in the sample without photocatalytic precursor is according to the reported in the bibliography after 10 h of irradiation, and even similar to CR and RhB samples where it is achieved around 40% in 20 h of exposition (see Figure 10a). However, the sample with the embedded metal oxide precursors (S4) has shown an almost total discoloration (90% of degradation rate) after 20 h of essay (Figure 10b), being the sample totally discolored in the incident area (Figure 10c). The FTIR spectra of the MB sample of both irradiated and non-irradiated are shown in Figure 10d. A peak in 2916 $cm^{-1}$ indicates a symmetrical stretching C-H of $CH_2$ band. The intense band in 1694 $cm^{-1}$ gives information about the presence of C=N and C=O vibrations in MB [59]. The transmittance peaks situated at 1158 and 1006 $cm^{-1}$ corresponds to the bending band of N-H and C-N from the amide band functional group [67,68]. As it has previously happened, an important reduction in the resultant intensities peak of the MB colorant after irradiation has been observed.

In Figure 11 is shown the whole photocatalytic tests performed to the MY azo-dye. After observing both Figure 11a (no presence of oxide precursors) and Figure 11b (immobilized photocatalytic precursors, S4 sample), it can be seen that a different dye degradation has been achieved with a rate of 15% and almost 60%, respectively. In addition, after light irradiation, black colored fibres have been obtained instead of a bright color aspect, as has occurred with the other dyes of this study (see Figure 11c). Finally, the FTIR spectra of MY azo dye can be visualized in Figure 11d where the main IR transmittance peaks corresponds to 1588 and 1142 $cm^{-1}$, related with the vibration modes of the azo bonds, which are associated to the N-H bending and C-O stretching functional groups, respectively. In addition, there is also a main peak in 3404 $cm^{-1}$ which is related to N-H stretching,

whereas the functional groups of S=O stretching are located at 1396 and 1031 $cm^{-1}$. The irradiated area has also exhibited a reduction intensity in transmittance as it has occurred with the previous dyes.

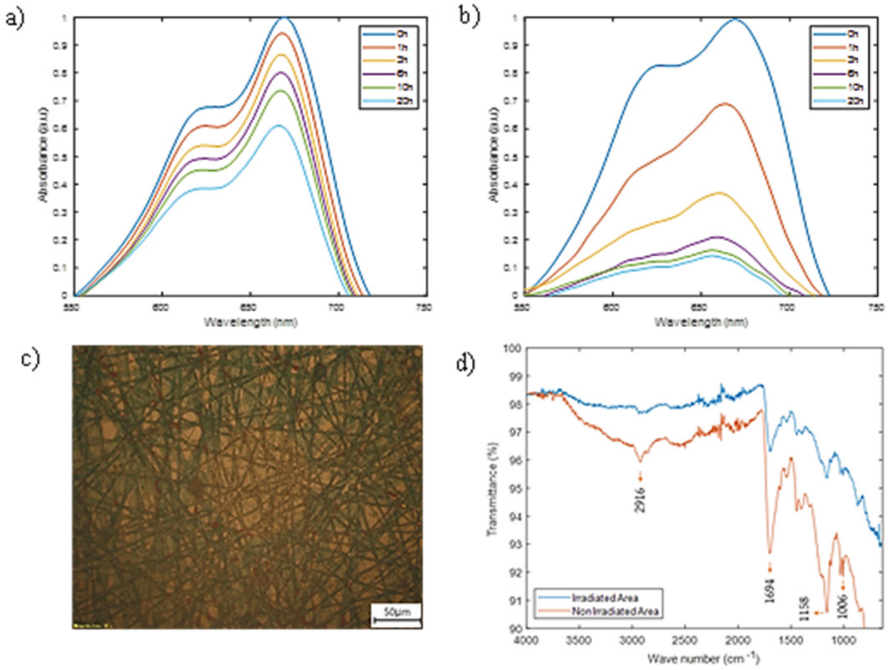


**Figure 10.** (**a**) Evolution of the degradation rate of MB deposited into sample S0 for a total irradiation time of 20 h; (**b**) evolution of the degradation rate of MB deposited into S4 sample for a total irradiation time of 20 h; (**c**) optical microscopy image of a micrometric degraded zone of the dye; (**d**) FTIR spectra of the irradiated and non-irradiated area of the Methylene Blue sample.

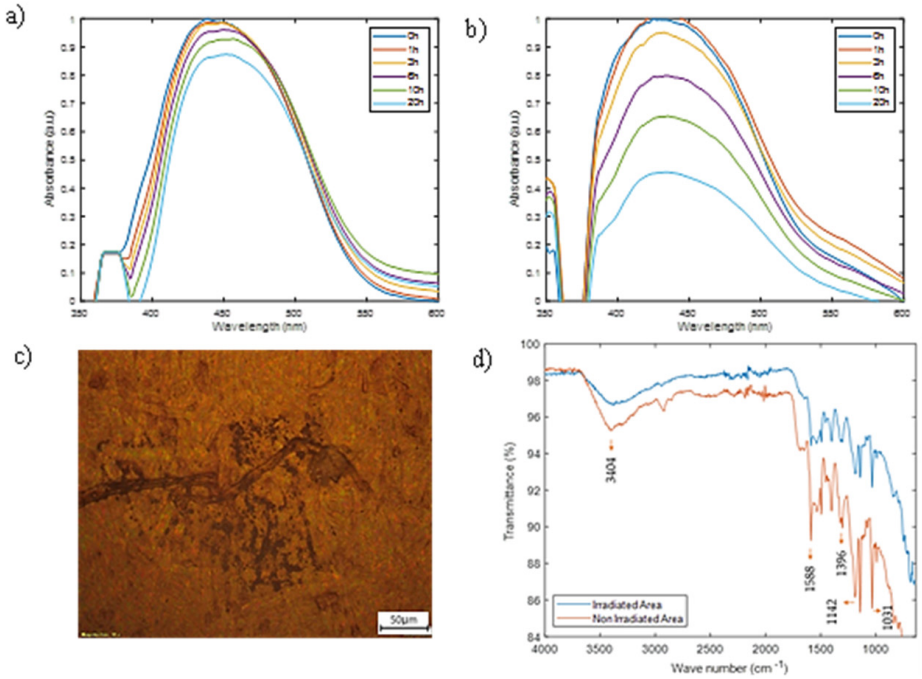


**Figure 11.** (**a**) Evolution of the degradation rate of MY deposited into sample S0 for a total irradiation time of 20 h; (**b**) evolution of the degradation rate of MY deposited into S5 sample for a total irradiation time of 20 h; (**c**) optical microscopy image of a micrometric degraded zone of the dye in sample S01; (**d**) FTIR spectra of the irradiated and non-irradiated area of the Metanil Yellow sample.

Finally, according to the photocatalytic experimental results, one of the main reasons of the higher photocatalytic efficiency of MG, RhB, and MB can be explained by the presence of $Cl^-$ ions, which have a tendency to ionize the photoinduced area of the coating, and exhibit a more positively charged molecule. Otherwise, CR and MY show a stronger bond of N=N, which can be also an important factor that contradicts the degradation of these dyes using $TiO_2$ and $Fe_2O_3$ photocatalytic precursors [69].

## 4. Conclusions

In this work, it has been corroborated how the photocatalytic activity dry test can be extended to other types of dyes, being a reliable evaluation method for the determination of the photocatalytic efficiency of functional coatings. This method could be an alternative to the actual aqueous photocatalytic efficiency determination essay. Different dyes can be easily immobilized into the functional coating, and the optical fibre based photocatalytic essay is intuitive and simple to carried out. This methodology is more sensitive with some dyes compared with others, not all of the colorants degrade in the same manner under the same conditions. The photocatalytic tests indicate that RhB has shown the highest degradation rate with a total discoloration of almost 95%, whereas MY has shown the lowest degradation rate with a total discoloration of almost 60%, respectively. In all cases, the FTIR spectra corroborate the reduction or even disappearance of the transmittance peaks in the irradiated area, being indicative of the breakage of molecular chains of the dyes. In this case, MG and MB present the major breakage of molecular chains after the 20 h photocatalytic test.

**Author Contributions:** Conceptualization, X.S., P.J.R. and R.R.; data curation, X.S.; investigation, X.S., J.E. and J.F.P.; methodology, P.J.R. and R.R.; project administration, P.J.R. and R.R.; validation, P.J.R. and R.R.; writing—original draft, X.S.; writing—review and editing, P.J.R. and R.R. All authors have read and agreed to the published version of the manuscript.

**Funding:** This research was funded by the Government of Navarra—Department of Economic Development (PC019/020 ARGITU).

**Institutional Review Board Statement:** Not applicable.

**Informed Consent Statement:** Not applicable.

**Data Availability Statement:** Not applicable.

**Conflicts of Interest:** The authors declare no conflict of interest.

## References

1. Mills, A. An overview of the methylene blue ISO test for assessing the activities of photocatalytic films. *Appl. Catal. B Environ.* **2012**, *128*, 144–149. [CrossRef]
2. Albistur, A.; Rivero, P.J.; Esparza, J.; Rodríguez, R. Evaluation of the photocatalytic activity and anticorrosion performance of electrospun fibers doped with metallic oxides. *Polymers* **2021**, *13*, 2011. [CrossRef] [PubMed]
3. Bafana, A.; Devi, S.S.; Chakrabarti, T. Azo dyes: Past, present and the future. *Environ. Rev.* **2011**, *19*, 350–370. [CrossRef]
4. Ismail, M.; Akhtar, K.; Khan, M.I.; Kamal, T.; Khan, M.A.; Asiri, A.M.; Seo, J.; Khan, S.B. Pollution, Toxicity and Carcinogenicity of Organic Dyes and their Catalytic Bio-Remediation. *Curr. Pharm. Des.* **2019**, *25*, 3645–3663. [CrossRef] [PubMed]
5. Raval, N.P.; Shah, P.U.; Shah, N.K. Malachite green "a cationic dye" and its removal from aqueous solution by adsorption. *Appl. Water Sci.* **2017**, *7*, 3407–3445. [CrossRef]
6. Haque, E.; Jun, J.W.; Jhung, S.H. Adsorptive removal of methyl orange and methylene blue from aqueous solution with a metal-organic framework material, iron terephthalate (MOF-235). *J. Hazard. Mater.* **2011**, *185*, 507–511. [CrossRef] [PubMed]
7. Mittal, A.; Gupta, V.K.; Malviya, A.; Mittal, J. Process development for the batch and bulk removal and recovery of a hazardous, water-soluble azo dye (Metanil Yellow) by adsorption over waste materials (Bottom Ash and De-Oiled Soya). *J. Hazard. Mater.* **2008**, *151*, 821–832. [CrossRef] [PubMed]
8. Mohan, S.V.; Bhaskar, Y.V.; Karthikeyan, J. Biological decolourisation of simulated azo dye in aqueous phase by algae Spirogyra species. *Int. J. Environ. Pollut.* **2004**, *21*, 211–222. [CrossRef]
9. Khataee, A.R.; Kasiri, M.B. Photocatalytic degradation of organic dyes in the presence of nanostructured titanium dioxide: Influence of the chemical structure of dyes. *J. Mol. Catal. A Chem.* **2010**, *328*, 8–26. [CrossRef]

10. Fujishima, A.; Rao, N.T.; Tryk, D.A. Titanium dioxide photocatalysis. *J. Photochem. Photobiol. C Photochem. Rev.* **2000**, *1*, 1–21. [CrossRef]
11. Lachheb, H.; Puzenat, E.; Houas, A.; Ksibi, M.; Elaloui, E.; Guillard, C.; Herrmann, J.M. Photocatalytic degradation of various types of dyes (Alizarin S, Crocein Orange G, Methyl Red, Congo Red, Methylene Blue) in water by UV-irradiated titania. *Appl. Catal. B Environ.* **2002**, *39*, 75–90. [CrossRef]
12. Piccinini, P.; Minero, C.; Vincenti, M.; Pelizzetti, E. Photocatalytic mineralization of nitrogen-containing benzene derivatives. *Catal. Today* **1997**, *39*, 187–195. [CrossRef]
13. Akpan, U.G.; Hameed, B.H. Parameters affecting the photocatalytic degradation of dyes using $TiO_2$-based photocatalysts: A review. *J. Hazard. Mater.* **2009**, *170*, 520–529. [CrossRef] [PubMed]
14. Ahmad, M.M.; Mushtaq, S.; Qahtani, H.S.A.; Sedky, A.; Alam, M.W. Investigation of $TiO_2$ Nanoparticles Synthesized by Sol-Gel Method for Effectual Photodegradation, Oxidation and Reduction Reaction. *Crystals* **2021**, *11*, 1456. [CrossRef]
15. Mendiola-Alvarez, S.Y.; Hernández-Ramírez, A.; Guzmán-Mar, J.L.; Maya-Treviño, M.L.; Caballero-Quintero, A.; Hinojosa-Reyes, L. A novel P-doped $Fe_2O_3$-$TiO_2$ mixed oxide: Synthesis, characterization and photocatalytic activity under visible radiation. *Catal. Today* **2019**, *328*, 91–98. [CrossRef]
16. Cao, Y.Q.; Zi, T.Q.; Zhao, X.R.; Liu, C.; Ren, Q.; Fang, J.B.; Li, W.M.; Li, A.D. Enhanced visible light photocatalytic activity of $Fe_2O_3$ modified $TiO_2$ prepared by atomic layer deposition. *Sci. Rep.* **2020**, *10*, 13437. [CrossRef]
17. Keerthana, S.P.; Yuvakkumar, R.; Ravi, G.; Kumar, P.; Elshikh, M.S.; Alkhamis, H.H.; Alrefaei, A.F.; Velauthapillai, D. A strategy to enhance the photocatalytic efficiency of $\alpha$-$Fe_2O_3$. *Chemosphere* **2021**, *270*, 129498. [CrossRef]
18. Souza, R.P.; Freitas, T.K.F.S.; Domingues, F.S.; Pezoti, O.; Ambrosio, E.; Ferrari-Lima, A.M.; Garcia, J.C. Photocatalytic activity of $TiO_2$, ZnO and $Nb_2O_5$ applied to degradation of textile wastewater. *J. Photochem. Photobiol. A Chem.* **2016**, *329*, 9–17. [CrossRef]
19. Khasawneh, O.F.S.; Palaniandy, P.; Palaniandy, P.; Ahmadipour, M.; Mohammadi, H.; Bin Hamdan, M.R. Removal of acetaminophen using $Fe_2O_3$-$TiO_2$ nanocomposites by photocatalysis under simulated solar irradiation: Optimization study. *J. Environ. Chem. Eng.* **2021**, *9*, 104921. [CrossRef]
20. Fawzi Suleiman Khasawneh, O.; Palaniandy, P. Removal of organic pollutants from water by $Fe_2O_3$/$TiO_2$ based photocatalytic degradation: A review. *Environ. Technol. Innov.* **2021**, *21*, 101230. [CrossRef]
21. Deb, H.; Xiao, S.; Morshed, M.N.; Al Azad, S. Immobilization of Cationic Titanium Dioxide ($TiO_{2+}$) on Electrospun Nanofibrous Mat: Synthesis, Characterization, and Potential Environmental Application. *Fibers Polym.* **2018**, *19*, 1715–1725. [CrossRef]
22. Ding, B.; Kim, J.; Kimura, E.; Shiratori, S. Layer-by-layer structured films of $TiO_2$ nanoparticles and poly (acrylic acid) on electrospun nanofibres. *Nanotechnology* **2004**, *15*, 913–917. [CrossRef]
23. Rivero, P.J.; Redin, D.M.; Rodríguez, R.J. Electrospinning: A powerful tool to improve the corrosion resistance of metallic surfaces using nanofibrous coatings. *Metals* **2020**, *10*, 350. [CrossRef]
24. Xue, J.; Xie, J.; Liu, W.; Xia, Y. Electrospun Nanofibers: New Concepts, Materials, and Applications. *Acc. Chem. Res.* **2017**, *50*, 1976–1987. [CrossRef] [PubMed]
25. Reneker, D.H.; Yarin, A.L. Electrospinning jets and polymer nanofibers. *Polymer* **2008**, *49*, 2387–2425. [CrossRef]
26. Huebner, A.L.; Chu, H.N. Instability and breakup of charged liquid jets. *J. Fluid Mech.* **1971**, *49*, 361–372. [CrossRef]
27. Deitzel, J.M.; Kleinmeyer, J.; Harris, D.; Beck Tan, N.C. The effect of processing variables on the morphology of electrospun. *Polymer* **2001**, *42*, 261–272. [CrossRef]
28. Richardson, J.J.; Cui, J.; Björnmalm, M.; Braunger, J.A.; Ejima, H.; Caruso, F. Innovation in Layer-by-Layer Assembly. *Chem. Rev.* **2016**, *116*, 14828–14867. [CrossRef]
29. Patrocinio, A.O.T.; Paula, L.F.; Paniago, R.M.; Freitag, J.; Bahnemann, D.W. Layer-by-Layer $TiO_2$/$WO_3$ Thin Films as Efficient Photocatalytic Self-Cleaning Surfaces. *ACS Appl. Mater. Interfaces* **2014**, *6*, 16859–16866. [CrossRef]
30. Rivero, P.J.; Garcia, J.A.; Quintana, I.; Rodriguez, R. Design of nanostructured functional coatings by usingwet-chemistry methods. *Coatings* **2018**, *8*, 76. [CrossRef]
31. Lipton, J.; Weng, G.M.; Röhr, J.A.; Wang, H.; Taylor, A.D. Layer-by-Layer Assembly of Two-Dimensional Materials: Meticulous Control on the Nanoscale. *Matter* **2020**, *2*, 1148–1165. [CrossRef]
32. Choi, J.; Rubner, M.F. Influence of the degree of ionization on weak polyelectrolyte multilayer assembly. *Macromolecules* **2005**, *38*, 116–124. [CrossRef]
33. Xie, A.F.; Granick, S. Weak versus strong: A weak polyacid embedded within a multilayer of strong polyelectrolytes. *J. Am. Chem. Soc.* **2001**, *123*, 3175–3176. [CrossRef]
34. Sharma, V.; Sundaramurthy, A. Multilayer capsules made of weak polyelectrolytes: A review on the preparation, functionalization and applications in drug delivery. *Beilstein J. Nanotechnol.* **2020**, *11*, 508–532. [CrossRef] [PubMed]
35. Xu, N.; Shen, X.; Cui, S.; Yi, X. Preparation of PAA/$WO_3$ composite films with enhanced electrochromism via layer-by-layer method. *IEEE J. Sel. Top. Quantum Electron.* **2018**, *25*, 565–569. [CrossRef]
36. Liu, Y.; Sun, D.; Askari, S.; Patel, J.; Macias-Montero, M.; Mitra, S.; Zhang, R.; Lin, W.F.; Mariotti, D.; Maguire, P. Enhanced Dispersion of $TiO_2$ Nanoparticles in a $TiO_2$/PEDOT:PSS Hybrid Nanocomposite via Plasma-Liquid Interactions. *Sci. Rep.* **2015**, *5*, 15765. [CrossRef]
37. Ahmad, J.; Deshmukh, K.; Habib, M.; Hägg, M.B. Influence of $TiO_2$ Nanoparticles on the Morphological, Thermal and Solution Properties of PVA/$TiO_2$ Nanocomposite Membranes. *Arab. J. Sci. Eng.* **2014**, *39*, 6805–6814. [CrossRef]

38. Shiratori, S.S.; Rubner, M.F. pH-dependent thickness behavior of sequentially adsorbed layers of weak polyelectrolytes. *Macromolecules* **2000**, *33*, 4213–4219. [CrossRef]
39. Lu, B.; Yuk, H.; Lin, S.; Jian, N.; Qu, K.; Xu, J.; Zhao, X. Pure PEDOT:PSS hydrogels. *Nat. Commun.* **2019**, *10*, 1043. [CrossRef]
40. Sandua, X.; Rivero, P.J.; Esparza, J.; Fernández-Palacio, J.; Conde, A.; Rodríguez, R.J. Design of Photocatalytic Functional Coatings Based on the Immobilization of Metal Oxide Particles by the Combination of Electrospinning and Layer-by-Layer Deposition Techniques. *Coatings* **2022**, *12*, 862. [CrossRef]
41. Ahmed, M.A.; El-Katori, E.E.; Gharni, Z.H. Photocatalytic degradation of methylene blue dye using $Fe_2O_3/TiO_2$ nanoparticles prepared by sol-gel method. *J. Alloys Compd.* **2013**, *553*, 19–29. [CrossRef]
42. Li, D.; Xia, Y. Electrospinning of nanofibers: Reinventing the wheel? *Adv. Mater.* **2004**, *16*, 1151–1170. [CrossRef]
43. Rivero, P.J.; Rosagaray, I.; Fuertes, J.P.; Palacio, J.F.; Rodríguez, R.J. Designing multifunctional protective PVC electrospun fibers with tunable properties. *Polymers* **2020**, *12*, 2086. [CrossRef] [PubMed]
44. Chau, T.T.; Bruckard, W.J.; Koh, P.T.L.; Nguyen, A.V. A review of factors that affect contact angle and implications for flotation practice. *Adv. Colloid Interface Sci.* **2009**, *150*, 106–115. [CrossRef] [PubMed]
45. Yoo, D.; Shiratori, S.S.; Rubner, M.F. Controlling bilayer composition and surface wettability of sequentially adsorbed multilayers of weak polyelectrolytes. *Macromolecules* **1998**, *31*, 4309–4318. [CrossRef]
46. Han, T.; Ma, Z.; Wang, D. Biofouling-Inspired Growth of Superhydrophilic Coating of Polyacrylic Acid on Hydrophobic Surfaces for Excellent Anti-Fouling. *ACS Macro Lett.* **2021**, *10*, 354–358. [CrossRef]
47. Xiangmei, L.; Junhui, H. Superhydrophilic and antireflective properties of silica nanoparticle coatings fabricated via layer-by-layer assembly and postcalcination. *J. Phys. Chem. C* **2009**, *113*, 148–152. [CrossRef]
48. Rampaul, A.; Parkin, I.P.; O'Neill, S.A.; DeSouza, J.; Mills, A.; Elliott, N. Titania and tungsten doped titania thin films on glass; active photocatalysts. *Polyhedron* **2003**, *22*, 35–44. [CrossRef]
49. Kontos, A.I.; Likodimos, V.; Stergiopoulos, T.; Tsoukleris, D.S.; Falaras, P.; Rabias, I.; Papavassiliou, G.; Kim, D.; Kunze, J.; Schmuki, P. Self-organized anodic $TiO_2$ nanotube arrays functionalized by iron oxide nanoparticles. *Chem. Mater.* **2009**, *21*, 662–672. [CrossRef]
50. Damchan, J.; Sikong, L.; Kooptarnond, K.; Niyomwas, S. Contact Angle of Glass Substrate Coated with $TiO_2/SiO_2$ Thin Film. *C. J. Nat. Sci. (Spec. Issue Nanotechnol.)* **2008**, *7*, 19–23.
51. Abou Neel, E.A.; Ahmed, I.; Blaker, J.J.; Bismarck, A.; Boccaccini, A.R.; Lewis, M.P.; Nazhat, S.N.; Knowles, J.C. Effect of iron on the surface, degradation and ion release properties of phosphate-based glass fibres. *Acta Biomater.* **2005**, *1*, 553–563. [CrossRef] [PubMed]
52. Güy, N.; Özacar, M. The influence of noble metals on photocatalytic activity of ZnO for Congo red degradation. *Int. J. Hydrogen Energy* **2016**, *41*, 20100–20112. [CrossRef]
53. Eskizeybek, V.; Sari, F.; Gülce, H.; Gülce, A.; Avci, A. Preparation of the new polyaniline/ZnO nanocomposite and its photocatalytic activity for degradation of methylene blue and malachite green dyes under UV and natural sun lights irradiations. *Appl. Catal. B Environ.* **2012**, *119–120*, 197–206. [CrossRef]
54. Zhuang, J.; Dai, W.; Tian, Q.; Li, Z.; Xie, L.; Wang, J.; Liu, P.; Shi, X.; Wang, D. Photocatalytic degradation of RhB over $TiO_2$ bilayer films: Effect of defects and their location. *Langmuir* **2010**, *26*, 9686–9694. [CrossRef] [PubMed]
55. Hunge, Y.M.; Mahadik, M.A.; Mohite, V.S.; Kumbhar, S.S.; Deshpande, N.G.; Rajpure, K.Y.; Moholkar, A.V.; Patil, P.S.; Bhosale, C.H. Photoelectrocatalytic degradation of methyl blue using sprayed $WO_3$ thin films. *J. Mater. Sci. Mater. Electron.* **2016**, *27*, 1629–1635. [CrossRef]
56. Masunga, N.; Mamba, B.B.; Kefeni, K.K. Trace samarium doped graphitic carbon nitride photocatalytic activity toward metanil yellow dye degradation under visible light irradiation. *Colloids Surfaces A Physicochem. Eng. Asp.* **2020**, *602*, 125107. [CrossRef]
57. Chen, C.C.; Lu, C.S.; Chung, Y.C.; Jan, J.L. UV light induced photodegradation of malachite green on $TiO_2$ nanoparticles. *J. Hazard. Mater.* **2007**, *141*, 520–528. [CrossRef]
58. Setyawati, H.; Darmokoesoemo, H.; Murwani, I.K.; Permana, A.J.; Rochman, F. Functionalization of Congo red dye as a light harvester on solar cell. *Open Chem.* **2020**, *18*, 287–294. [CrossRef]
59. Bartošová, A.; Blinová, L.; Sirotiak, M.; Michalíková, A. Faculty of Materials Science and Technology in Trnava Usage of Ftir-Atr As Non-Destructive Analysis of Selected Toxic Dyes. *Rput* **2017**, *25*, 103–111.
60. Oliveira, J.A.; Nogueira, A.E.; Gonçalves, M.C.P.; Paris, E.C.; Ribeiro, C.; Poirier, G.Y.; Giraldi, T.R. Photoactivity of N-doped ZnO nanoparticles in oxidative and reductive reactions. *Appl. Surf. Sci.* **2018**, *433*, 879–886. [CrossRef]
61. Soo, J.A.L.; Shoparwe, N.F.; Otitoju, T.A.; Mohamad, M.; Tan, L.S.; Li, S.; Makhtar, M.M.Z. Characterization and kinetic studies of poly (Vinylidene fluoride-co-hexafluoropropylene) polymer inclusion membrane for the malachite green extraction. *Membranes* **2021**, *11*, 676. [CrossRef] [PubMed]
62. Mukherjee, G.; Biradha, K. 1D, 2D and 3D coordination polymers of 1,3-phenylene diisonicotinate with Cu(i)/Cu(ii): $Cu_2I_2$ building block, anion influence and guest inclusions. *Cryst. Eng. Comm.* **2014**, *16*, 4701–4705. [CrossRef]
63. Zetra, Y. Photocatalytic degradation of malachite green using $TiO_2$ and $O_2$/UV Photocatalytic Degradation of Malachite Green using $TiO_2$. *AIP Conf. Proc.* **2020**, 020092.
64. Kang, W.; Gao, Y.; Tang, X.; Cao, C.; Hu, L.; Yang, H. Polymer concentration detection method based on fluorescent polymer to evaluate its retention and percolation. *J. Appl. Polym. Sci.* **2019**, *136*, 47468. [CrossRef]

65. Lamdab, U.; Wetchakun, K.; Kangwansupamonkon, W.; Wetchakun, N. Effect of a pH-controlled co-precipitation process on rhodamine B adsorption of $MnFe_2O_4$ nanoparticles. *RSC Adv.* **2018**, *8*, 6709–6718. [CrossRef]
66. Mathurasa, L.; Damrongsiri, S. Low cost and easy rice husk modification to efficiently enhance ammonium and nitrate adsorption. *Int. J. Recycl. Org. Waste Agric.* **2018**, *7*, 143–151. [CrossRef]
67. Xia, Y.; Yao, Q.; Zhang, W.; Zhang, Y.; Zhao, M. Comparative adsorption of methylene blue by magnetic baker's yeast and EDTAD-modified magnetic baker's yeast: Equilibrium and kinetic study. *Arab. J. Chem.* **2019**, *12*, 2448–2456. [CrossRef]
68. Mahmoud, M.E.; Yakout, A.A.; Osman, M.M. Dowex anion exchanger-loaded-baker's yeast as bi-functionalized biosorbents for selective extraction of anionic and cationic mercury(II) species. *J. Hazard. Mater.* **2009**, *164*, 1036–1044. [CrossRef]
69. Kadiya, K.; Vuggili, S.B.; Gaur, U.K.; Sharma, M. Comparative photocatalytic dye and drug degradation study using efficient visible light–induced silver phosphate nanoparticles. *Environ. Sci. Pollut. Res.* **2020**, *28*, 46390–46403. [CrossRef]